Journal of Materials Chemistry A

ROYAL SOCIETY OF CHEMISTRY

PAPER

View Article Online
View Journal | View Issue

Check for updates

Cite this: *J. Mater. Chem. A*, 2025, **13**, 30167

In ambient air processed Cu_2ZnSnS_4 absorber layers from DMSO-based precursors: enhanced efficiency *via* device post-annealing

Achmad Nasyori, *[a] Maris Pilvet, [a] Annabel Saar,[a] Jüri Krustok, [a] Mati Danilson, [a] Reelika Kaupmees, [a] Valdek Mikli, [a] Yuancai Gong, [cd] Raavo Josepson,[b] Edgardo Saucedo, [cd] Maarja Grossberg-Kuusk [a] and Marit Kauk-Kuusik [a]

Received 5th June 2025
Accepted 15th August 2025

DOI: 10.1039/d5ta04554a

rsc.li/materials-a

Solution-based processes have gained considerable attention as promising route toward high-efficiency kesterite-based photovoltaics. Dimethyl sulfoxide (DMSO) is commonly utilized as a solvent because of its low toxicity and exceptional solvating power, attributed to its high polarity, high dielectric constant, and strong Lewis base. However, most DMSO-based kesterite syntheses are conducted in glove boxes under inert gas atmosphere, increasing complexity and cost. In this work, we present precursor engineering strategies and simple post-annealing of device approach for fabricating high-performance Cu_2ZnSnS_4 (CZTS) solar cells using DMSO under ambient air. Four distinct precursor formulations were investigated, and a tailored post-annealing treatment was developed for the complete device to enhance the fill factor (FF) and overall power conversion efficiency (PCE). Post-annealing at 300 °C for 12 minutes in ambient air significantly enhanced device performance, yielding a PCE of 9.4% and increasing the FF from 33.0% to 62.0%. Comprehensive structural and optoelectronic characterization revealed improved heterojunction formation after the post-annealing. To the best of our knowledge, this represents the highest reported efficiency for CZTS solar cells without any alloying fabricated using DMSO under ambient air conditions. These findings demonstrate a cost-effective and scalable fabrication route and highlight the crucial role of device post-annealing in achieving high-efficiency air-processed CZTS solar cells.

1. Introduction

Meeting future global energy demand depends on the development of sustainable and scalable technologies that prioritize environmental compatibility, material abundance, and non-toxicity. Among next-generation photovoltaic (PV) materials, kesterite-based compounds—Cu_2ZnSnS_4 (CZTS), $Cu_2ZnSnSe_4$ (CZTSe), and their solid solutions $Cu_2ZnSn(S,Se)_4$ (CZTSSe) have emerged as promising candidates for cost-effective thin-film solar cells. These quaternary chalcogenides are derived from the chalcopyrite structure of CIGS ($Cu(In,Ga)(S,Se)_2$), replacing scarce and expensive In and Ga with earth-abundant and benign elements Zn and Sn. In addition to their favourable chemistry, CZTS has a direct bandgap of ~1.5 eV and a high absorption coefficient ($>10^4$ cm^{-1}), making it an ideal absorber for single-junction PV applications. The optical bandgap of CZTS can be fine-tuned between 1.5 and 2.1 eV through compositional alloying (*e.g.*, with Ge or Ag), enabling its use not only as a wide-bandgap absorber in tandem architectures with bottom cells of crystalline silicon or perovskite, but also in indoor photovoltaic (IPV) applications, where higher bandgaps are advantageous for harvesting indoor lighting efficiently. So far, the highest performance of the solar cells based on CZTS materials is over 13%, which is attained by the solution-processed technique.[1–5]

Solution processing typically involves dissolving metal salt precursors in a solvent to form a homogeneous ink, which is subsequently deposited using techniques such as spin coating or spray coating, followed by a short annealing treatment at high temperature to form the crystalline absorber and remove organic residues. The pioneering work by Mitzi's group at IBM demonstrated a record 12.6% CZTSSe solar cell using hydrazine-based solvents.[1,5,6] However, the high toxicity and instability of hydrazine have prompted researchers to pursue

---

[a] *Department of Materials and Environmental Technology, Tallinn University of Technology, Ehitajate tee 5, 19086 Tallinn, Estonia. E-mail: achmad.nasyori@taltech.ee*

[b] *Division of Physics, Tallinn University of Technology, Ehitajate tee 5, 19086 Tallinn, Estonia*

[c] *Electronic Engineering Department, Universitat Politècnica de Catalunya (UPC), Photovoltaic Lab – Micro and Nano Technologies Group (MNT), EEBE, Av Eduard Maristany 10-14, Barcelona 08019, Catalonia, Spain*

[d] *Barcelona Center for Multiscale Science & Engineering, Universitat Politècnica de Catalunya (UPC), Av Eduard Maristany 10-14, Barcelona 08019, Catalonia, Spain*

greener alternatives. A key advancement in this direction came with the use of dimethyl sulfoxide (DMSO) as a less-toxic alternative to dimethylformamide (DMF) and 2-methoxyethanol (MOE), and an effective polar coordinating solvent.[7–9] Hillhouse and colleagues first demonstrated 4% efficiency using DMSO-based CZTS solutions, later improved to 8% by optimizing precursor chemistry and annealing protocols.[7,8] Haass *et al.* further pushed the efficiency of DMSO-processed CZTSSe to 12% by engineering sodium doping and multistep selenization.[9] In parallel, the work of Xin's group emphasized the use of Sn^{4+} salts over Sn^{2+} to suppress secondary phases during high-temperature annealing, enabling efficiencies exceeding 14%.[10–13] Several published studies on kesterite solar cells using DMSO as the primary solvent are summarized in Table S1 (SI).

Despite these advancements, most high-performing DMSO-based CZTSSe devices have been fabricated under inert gas (glovebox) conditions to minimize oxidation, solvent degradation, and film inhomogeneity during deposition. This requirement increases processing complexity and cost, posing challenges for industrial scalability. Therefore, developing DMSO-based solution processing strategies that are compatible with ambient air conditions is crucial for transitioning kesterite photovoltaics toward commercial viability. To date, the highest reported efficiency for air-fabricated, DMSO-processed pure CZTS solar cells is 4.7%, obtained by Engberg *et al.*[14] This value is lower than CZTSSe, with 11.3% efficiency reported by Haass *et al.*[9] Efforts to overcome ambient air sensitivity have included combining DMSO with co-solvents such as dimethylformamide (DMF),[15,16] 2-methoxyethanol (MOE),[17] or water,[18] as well as employing targeted post-annealing treatments to improve crystallinity and reduce defect density.[12,19]

Post-annealing or thermal treatment has emerged as a pivotal step in the fabrication of high-performance kesterite solar cells. This post-annealing technique is widely employed to enhance fill factor (FF), reduce interface recombination, and improve the overall power conversion efficiency (PCE).[19] Various research groups have demonstrated that carefully optimized annealing parameters, such as temperature, duration, and ambient conditions, can significantly influence the absorber/buffer interface, promote beneficial elemental diffusion, and suppress detrimental secondary phases.[19–28] For example, Hao *et al.* reported a co-sputtered CZTS absorber that, upon annealing of the CZTS/CdS heterojunction at 270 °C for 10 min in N_2 atmosphere, achieved a PCE increase from 7.8% to 11.0% and FF from 56.3% to 69.3%.[19] Similarly, Liu *et al.* applied a post-deposition annealing in argon atmosphere at 300 °C for 8 min on solution-processed kesterite devices, improving efficiency from 6.7% to 10.9% and FF from 62% to 68%.[25] In our previous work on CZTS monograin powder, annealing in ambient air at temperatures between 175–275 °C for 10 min led to a moderate efficiency improvement from 6.7% to 7.3%.[29] Gong *et al.* demonstrated a notable performance boost up to 13% and FF of 73.4% *via* post-annealing at 110 °C for 12 hours in a glovebox environment.[11,12] These findings collectively affirm the effectiveness of post-annealing in enhancing FF and device performance. However, studies focused on post-annealing of devices under ambient air conditions for solution-based CZTS absorbers remain scarce.

This work presents a systematic study of air-processed, solution-based CZTS solar cells using DMSO under ambient air. By optimizing four metal salt precursor chemistries, we have eliminated worm-like morphologies and achieved uniform absorber films. Post-annealing of the full device at 300 °C for 12 min significantly boosted the fill factor and power conversion efficiency (PCE), yielding a champion device with 9.4% PCE. To the best of our knowledge, this is the highest efficiency reported for pure CZTS solar cells fabricated from DMSO under ambient conditions. These results highlight a scalable, glovebox-free route toward high-performance, sustainable thin-film photovoltaics.

2. Materials and methods

2.1. Materials and solution preparation

Four precursor solutions were prepared under ambient conditions at room temperature using dimethyl sulfoxide (DMSO) as the solvent. The precursor materials, summarized in Table 1, were adopted from previous studies.[9–11] The molar ratios were adjusted to maintain Cu/(Zn + Sn) = 0.85, Zn/Sn = 1.2, and TU/(Cu + Zn + Sn) = 2.0. Specifically, 40.7 mmol of thiourea (TU), 9.35 mmol of Cu, 5 mmol of Sn, 6 mmol of Zn, and 10 mL of DMSO were added to a vial. Each solution was stirred at 65 °C until complete dissolution was achieved.

2.2. CZTS thin-film preparation

CZTS thin films were deposited on Mo-coated soda lime glass substrates *via* spin coating under ambient conditions. The precursor solutions were filtered through a 0.45 μm disposable syringe filter prior to sequential spin-coating. The precursor film was annealed on a hotplate at 350 °C for 2 minutes, followed by a 5 minutes cooling period. This process was performed eight coating cycles to obtain the desired absorber thickness (~1.2 μm). Subsequently, the sulfurization process was carried out in a graphite box ($V = 36\ cm^3$, 6 cm × 6 cm × 1 cm) containing 200 mg of sulphur, using an OTF-1200X tube furnace. The temperature was ramped to 650 °C within 32.5 minutes and held at the target temperature for 20 minutes under an Ar atmosphere at a pressure of 6.5×10^2 Torr. For clarity in the analysis and discussion, CZTS precursor films before sulfurization are denoted as PF, and the resulting CZTS thin film after sulfurization as TF.

Table 1 Precursor materials used in each spin-coating solution for CZTS thin-film preparation

Solution	Copper	Zinc	Tin	Sulphide
Sol-1	CuCl	Zn (Ac)$_2$	$SnCl_4\cdot 5H_2O$	Thiourea
Sol-2	CuCl	$ZnCl_2$	$SnCl_2\cdot 2H_2O$	Thiourea
Sol-3	$CuCl_2\cdot 2H_2O$	Zn (Ac)$_2$	$SnCl_4\cdot 5H_2O$	Thiourea
Sol-4	$CuCl_2\cdot 2H_2O$	$ZnCl_2$	$SnCl_2\cdot 2H_2O$	Thiourea

2.3. CZTS solar cell preparation

The sulfurized CZTS thin films were immersed in ultrapure water (~18.2 MΩ cm) for 4 min and then transferred to a beaker maintained at 60 °C for chemical bath deposition (CBD).[30] The CBD solution contained 0.02 M cadmium acetate ($CdAc_2$), 0.35 M thiourea, and 2 M aqueous ammonia solution (NH_4OH). CBD was conducted under continuous stirring for 8 min, resulting in a CdS layer approximately ~40–60 nm thick. Then, ~50 nm of i-ZnO and ~250 nm of ITO was deposited by radio frequency magnetron sputtering. Post-annealing of the complete devices (Mo/CZTS/CdS/i-ZnO/ITO) was conducted in ambient air on hotplate at 300 °C for 10, 12, and 15 min using a graphite box. An illustration of the preparation process is provided in Fig. 1.

2.4. Characterization techniques

The structural, morphological, compositional, and optoelectronic properties of both as-deposited and sulfurized CZTS absorber layers were systematically analysed. High-resolution scanning electron microscopy (HR-SEM, Zeiss Ultra 55) equipped with a backscattered electron detector was used for morphological analysis. Elemental composition was determined *via* energy-dispersive X-ray spectroscopy (EDX, Bruker Esprit 1.82) with an EDX-Xflash 3001 detector. Raman spectra were acquired at room-temperature using a HORIBA LabRAM 800HR Micro-Raman spectrometer, with a 532 nm Nd:YAG laser as the excitation source. The scattered light was analysed using an 1800 lines per mm grating monochromator and a Si CCD detector. Crystallographic properties were examined *via* X-ray diffraction (XRD) using a Rigaku Ultima IV diffractometer equipped with a 9 kW rotating Cu anode ($\lambda = 0.154$ nm, 40 kV, 40 mA) in Bragg–Brentano geometry (2θ range: 10–70°, step size: 0.02°) with a silicon strip detector (D/teX Ultra). For device characterization, current density–voltage (J–V) measurements were performed under standard test conditions (AM 1.5, 100 mW cm^{-2}) using a Newport Oriel Class A 91195A solar simulator. External quantum efficiency (EQE) spectra were recorded using a commercial EQE measurement system (Sciencetech Inc., PTS-2-IQE, Canada). Capacitance–frequency, impedance spectroscopy, and temperature-dependent IV characteristics were measured using a Wayne Kerr 6500B impedance analyser, a closed system He cryostat (Janis), and a Keithley 2400 source meter.

3. Result and discussion

3.1. Characterization of CZTS precursor films

The use of DMSO as a solvent under ambient conditions often results in the formation of a distinct worm-like surface pattern on the precursor films.[14,17] This phenomenon is likely attributed to the presence of excessive organic residues in the precursor film and the high sensitivity of DMSO to atmospheric oxygen during the spin coating process. The interaction of DMSO with ambient oxygen may lead to microstructural inhomogeneities, increased surface roughness, and particle aggregation,

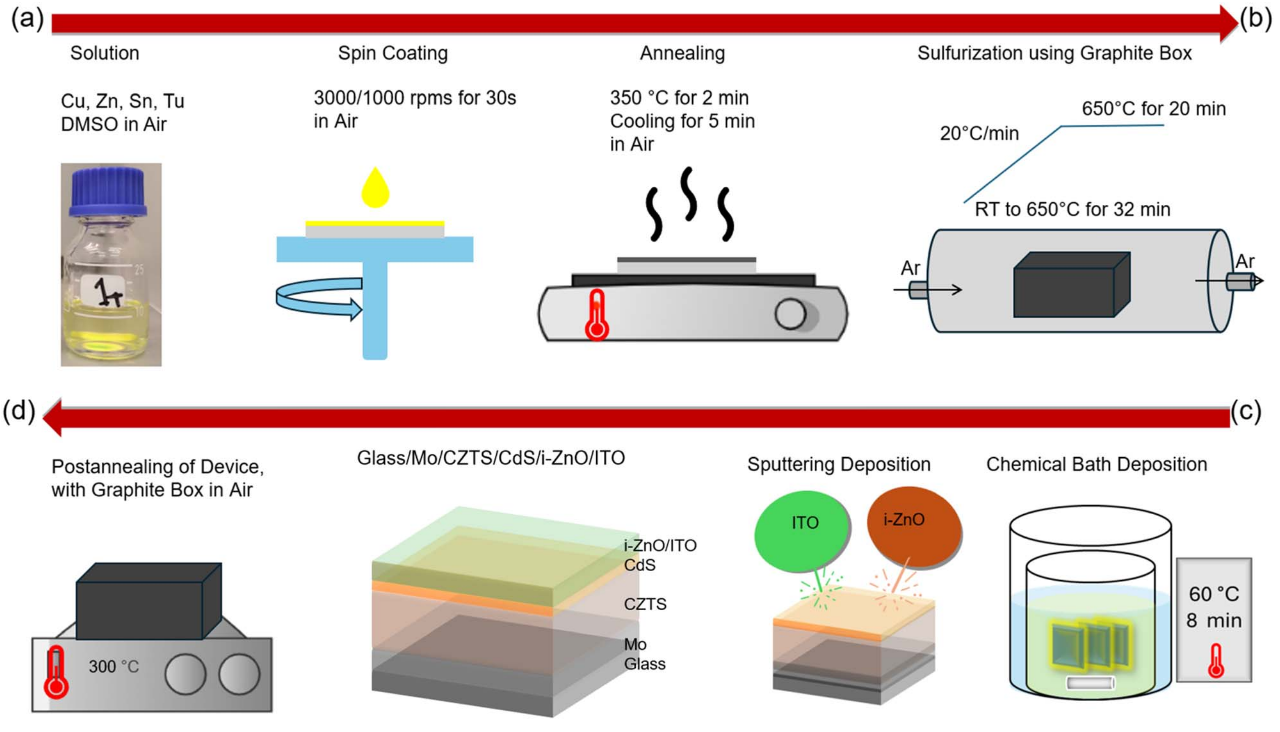

Fig. 1 Schematic illustration of the fabrication process for solution-processed CZTS solar cells. (a) and (b) Preparation of CZTS absorber layer: the precursor solution was formulated in DMSO, followed by spin coating, brief annealing on a hotplate, and high-temperature sulfurization in a graphite box using a tube furnace. (c) and (d) Device fabrication steps: chemical bath deposition (CBD) of CdS buffer layer, RF sputtering of intrinsic ZnO and ITO as window layers, and post-annealing of the device on a hotplate inside a graphite enclosure under ambient conditions.

potentially facilitating the formation of secondary phases.[14–17] These factors suggest that the direct use of DMSO as a single solvent under ambient conditions may be suboptimal for achieving smooth and uniform CZTS precursor films. To mitigate these morphological issues, solvent engineering strategies have been investigated, including blending DMSO with co-solvents such as dimethylformamide (DMF),[15,16] 2-methoxyethanol (MOE),[17] and water (H_2O),[18] which have been shown to improve film uniformity and morphology.

The morphological characteristics of CZTS precursor films were investigated using SEM, as shown in Fig. 2a–c, which present images of the CZTS precursor films at various magnifications. As shown in Fig. 2c (500×), only the PF-3 film-prepared using $CuCl_2\cdot 2H_2O$, $ZnCl_2$, $SnCl_2\cdot 2H_2O$, and Tu-exhibited a worm-like surface pattern, whereas PF-1 and PF-2 films showed more uniform morphologies. This suggests that appropriate precursor selection materials and control over processing parameters, such as annealing temperature during precursor film preparation, plays a key role in suppressing the formation of worm-like patterns.[14] At low magnifications (500× and 5000×), the surface morphologies of all precursor films appeared relatively similar, however, higher magnification (50 000×) revealed notable differences. The PF-2 film exhibited early-stage crystallization after short annealing at 350 °C, with the formation of small CZTS grains, while PF-1 and PF-3 remained predominantly amorphous. These results highlight the critical role of precursor composition in influencing both crystallinity and surface morphology-factors that are crucial for fabrication of high-quality CZTS absorber layer.

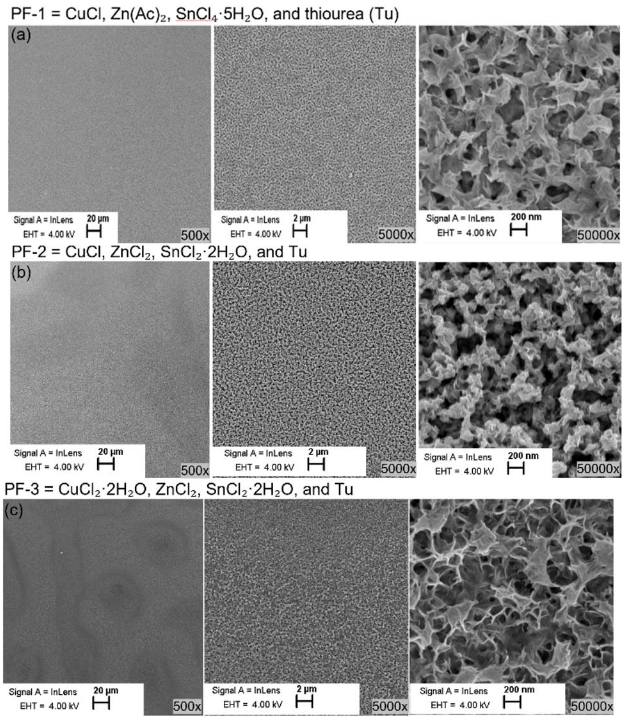

Fig. 2 Top-view SEM images of CZTS precursor films (PF): (a) PF-1, (b) PF-2, and (c) PF-3, each shown at magnifications of 500×, 5000×, and 50 000×. All precursor films were air-annealed at 350 °C for 2 minutes and cooled for 5 minutes, with the cycle repeated eight times.

Fig. 3 presents the Raman spectra of CZTS precursor films prepared from different precursor solutions. The precursor film based on Sol-4 was excluded from further analysis due to incomplete precursor dissolution, which led to the formation of white suspensions. Raman spectra of precursor films (PF-1, PF-2, and PF-3) exhibit broad Raman peaks cantered around 331 cm^{-1}, characteristic of CZTS, indicating the amorphous nature of the as-deposited films. It is noteworthy that no Cu_2S secondary phases were detected in any of the precursor films, including PF-2, which was prepared using a Sn^{2+}-based precursor. This finding contrasts with the results reported by Gong *et al.*,[10,11] who observed that Sn^{4+} precursors suppress Cu_2S formation more effectively than Sn^{2+}. These results suggest that the formation of Cu_2S is not an inevitable outcome when fabricating CZTS using Sn^{2+}-based precursor. Instead, it may depend on variations in precursor ratios and solution preparation conditions. Furthermore, the presence of ZnS was detected in all precursor films, which is expected due to the Zn-rich composition. Therefore, the chemical reactions from the precursor solutions (Sol-1, Sol-2, and Sol-3) to the corresponding CZTS precursor films can be represented as follows:

Precursor solution formation in DMSO:

1. Metal ions form thiourea (Tu) complexes:

$$\mathrm{CuCl} + 3\mathrm{Tu} \rightarrow \mathrm{Cu(Tu)_3Cl} \tag{1.1}$$

$$\mathrm{CuCl_2\cdot 2H_2O} + 3\mathrm{Tu} \rightarrow \mathrm{Cu(Tu)_3Cl_2} \tag{1.2}$$

$$\mathrm{Zn(OAc)_2} + 2\mathrm{Tu} \rightarrow \mathrm{Zn(Tu)_2(OAc)_2} \tag{1.3}$$

$$\mathrm{ZnCl_2} + 2\mathrm{Tu} \rightarrow \mathrm{Zn(Tu)_2Cl_2} \tag{1.4}$$

$$\mathrm{SnCl_4\cdot 5H_2O} + x\mathrm{Tu} \rightarrow \mathrm{Sn(Tu)}_x\mathrm{Cl_4} \tag{1.5}$$

$$\mathrm{SnCl_2\cdot 2H_2O} + x\mathrm{Tu} \rightarrow \mathrm{Sn(Tu)}_x\mathrm{Cl_2} \tag{1.6}$$

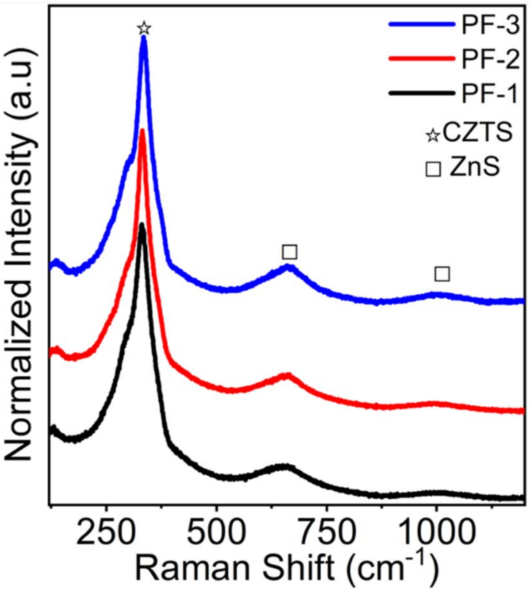

Fig. 3 Raman spectra of CZTS precursor film (PF) before sulfurization, prepared from different solutions: PF-1, PF-2, and PF-3.

These complexes are soluble in DMSO, stabilizing the metals in the solution.

2. Formation of binary metal sulphides:

$$\mathrm{Cu(Tu)_3Cl_2 \rightarrow CuS\ or\ Cu_2S} \tag{2.1}$$

$$\mathrm{Cu(Tu)_3Cl \rightarrow CuS\ (or\ Cu_2S)} \tag{2.2}$$

$$\mathrm{Zn(Tu)_2Cl_2 \rightarrow ZnS} \tag{2.3}$$

$$\mathrm{Zn(Tu)_2(OAc)_2 \rightarrow ZnS} \tag{2.4}$$

$$\mathrm{Sn(Tu)}_x\,\mathrm{Cl_2\ or\ Sn(Tu)}_x\mathrm{Cl_4 \rightarrow SnS\ or\ SnS_2}\quad (\mathrm{Sn^{2+}}\text{ typically forms SnS, not }\mathrm{SnS_2}) \tag{2.5}$$

The binary sulphides react to form the quaternary CZTS phase:

$$\mathrm{2CuS + ZnS + SnS + S \rightarrow Cu_2ZnSnS_4\ or\ Cu_2S + ZnS + SnS + S \rightarrow Cu_2ZnSnS_4} \tag{3}$$

Chemical reaction of Sol-1.[10,11,31–33]

$$\mathrm{Cu(Tu)_3Cl + Zn(Tu)_2(OAc)_2 + Sn(Tu)}_x\mathrm{Cl_4 \rightarrow Cu_2ZnSnS_4 + ZnS} \tag{4}$$

Chemical reaction of Sol-2.[10,11]

$$\mathrm{Cu(Tu)_3Cl + Zn(Tu)_2Cl_2 + Sn(Tu)}_x\mathrm{Cl_2 \rightarrow Cu_2ZnSnS_4 + ZnS} \tag{5}$$

Chemical reaction of Sol-3.[10,11,31–33]

$$\mathrm{Cu(Tu)_3Cl_2 + Zn(Tu)_2(OAc)_2 + Sn(Tu)}_x\mathrm{Cl_4 \rightarrow Cu_2ZnSnS_4 + ZnS} \tag{6}$$

3.2. Characterization of sulfurized CZTS thin films

To gain deeper insight into the crystallization behaviour, top-view and cross-sectional SEM analysis were performed on TF-1, TF-2, and TF-3 films after sulfurization at 650 °C for 20 minutes (Fig. 4). TF-1 and TF-3 films exhibited incomplete crystallization, characterised by small grains and numerous grain boundaries in both surface (Fig. 4a and c) and cross-sectional views (Fig. 4d and f), indicating poor crystallinity. In contrast, TF-2 demonstrated well-defined, large grains and a compact, uniform structure throughout the film thickness (Fig. 4b and e), indicating that sulfurization at 650 °C for 20 minutes was sufficient to achieve high crystallinity. This superior morphology highlights TF-2 film's potential for enhanced photovoltaic performance, as improved crystallinity and enlarged grain size are expected to reduce recombination losses and facilitate efficient charge transport within the CZTS films.

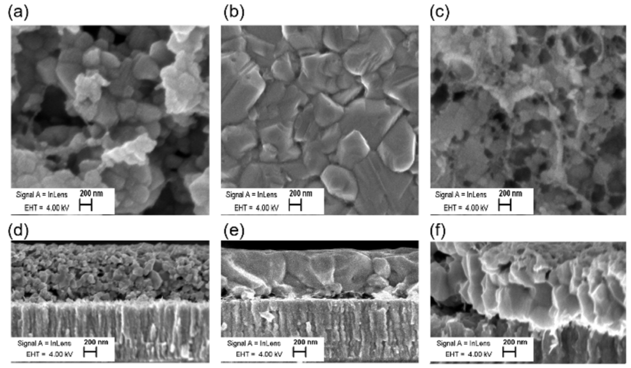

Fig. 4 Top-view (a) TF-1, (b) TF-2, and (c) TF-3, and cross-sectional view (d) TF-1, (e) TF-2, and (f) TF-3, SEM images of the CZTS thin film (TF) annealed at 650 °C for 20 min.

Fig. 5a shows the Raman spectra of all CZTS thin films after sulfurization at 650 °C for 20 minutes. The TF-1, TF-2, and TF-3 films exhibit well defined peaks, indicating successful crystallization of the kesterite phase. A strong CZTS peak is observed at 336 $\mathrm{cm^{-1}}$ in all three films, which is characteristic of the A1 vibrational mode of the kesterite structure. In addition to the main peak, low-intensity peak appears at 286 $\mathrm{cm^{-1}}$ and 373 $\mathrm{cm^{-1}}$. The inset of Fig. 5a shows the full width at half maximum (FWHM) of the 336 $\mathrm{cm^{-1}}$ peak for each sample. Among the three films, TF-2 demonstrates the sharpest peak with the lowest FWHM value of 3.4 $\mathrm{cm^{-1}}$. In comparison, TF-3 and TF-1 exhibit broader peaks with FWHM values of 8.4 $\mathrm{cm^{-1}}$ and 10.4 $\mathrm{cm^{-1}}$, respectively. Generally, a narrower FWHM in Raman spectra is associated with improved crystal quality. Therefore, the data suggest that TF-2 possesses the best crystalline quality among the investigated films, which could be advantageous for subsequent device performance. Fig. 5b displays the XRD patterns of the precursor film and the sulfurized films. The precursor film does not exhibit any significant crystalline CZTS phase, indicating that it is primarily amorphous or consists of poorly crystalline phases. In contrast, the sulfurized thin films display prominent diffraction peaks at 18.3°, 28.4°, 33.0°, 47.3°, and 56.2° correspond to the (101), (112), (200), (220), and (312) planes of the kesterite CZTS phase, consistent with literature reports.[11,17,34] XRD analysis also reveals the presence of SnS as a secondary phase in all CZTS thin films, which may result from the decomposition of Sn compounds due to pressure reduction following high-temperature sulfurization.[35] Additionally, the formation of $\mathrm{MoS_2}$ is detected after sulfurization, likely due to the elevated sulfurization temperature and the sulphur-rich annealing environment.[9] For clarity, the chemical reactions during sulfurization can be seen as follows:

Reaction of PF-1, PF-2, and PF-3 during sulfurization

$$\mathrm{Cu_2ZnSnS_4 + S \rightarrow Cu_2ZnSnS_4} \tag{7}$$

$$\mathrm{Mo + 2S \rightarrow MoS_2} \tag{8}$$

Subsequently, elemental analysis by energy-dispersive X-ray spectroscopy (EDX) before and after sulfurization (650 °C, 20 min) revealed significant compositional changes in the CZTS absorber layers (Table 2), directly influencing film stoichiometry and device quality, for example. Notably, in PF-2 and TF-2, the Cu content increased from 20.3 at% to 21.4 at% after sulfurization, likely due to improved Cu quantity under sulphur-

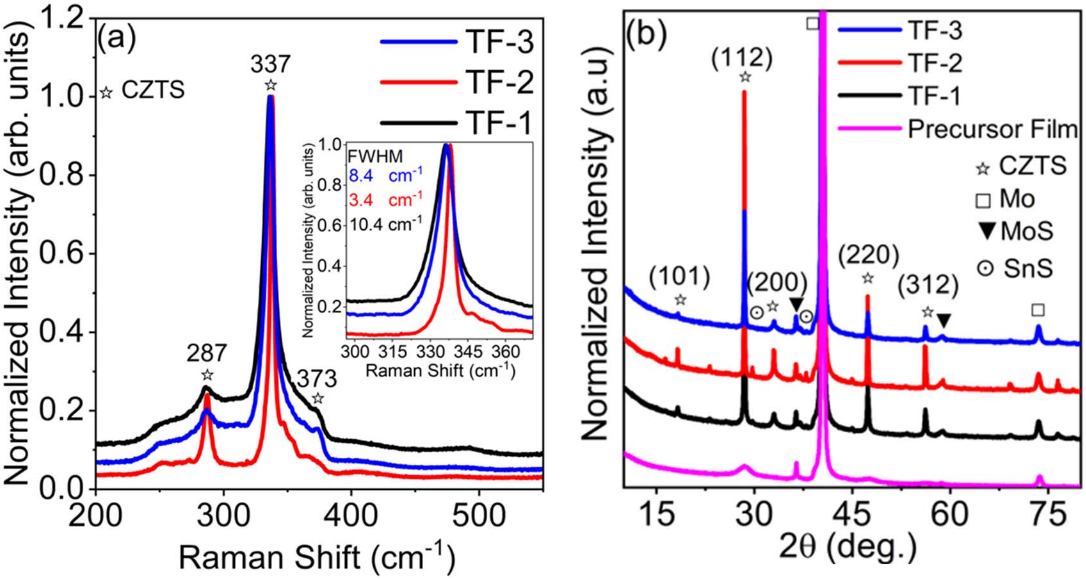

Fig. 5 (a) Raman spectra of CZTS thin films (TF) after sulfurization, corresponding to TF-1, TF-2, and TF-3. (b) XRD patterns of CZTS thin films (TF) from different solutions: TF-1, TF-2, and TF-3. The sulfurization process was conducted at 650 °C for 20 minutes.

rich conditions. This adjustment optimized the Cu/(Zn + Sn) ratio to 0.89, aligning closely with the optimal range for single-phase kesterite formation.[10–12] In contrast, both Zn and Sn content decreased across all CZTS thin films, attributed to the thermal volatility of Sn compounds, which may compromise phase stability and introduce deep-level defects. Among the tested absorbers, Sol-2 based precursor film and thin film exhibited the most favourable elemental distribution, with Cu/(Zn + Sn) and Zn/Sn ratios aligning with theoretical targets for high-performance CZTS solar cells.

In summary, TF-2 exhibited superior crystallinity, as evidenced by SEM images showing large, well-defined grains with low grain boundary density, favourable for efficient charge transport. Raman spectroscopy confirmed high structural quality, showing sharp and intense peaks at 337 cm^{-1}, 286 cm^{-1}, and 373 cm^{-1}. XRD analysis further supported these observations, revealing strong, well-defined peaks assigned to the (101), (112), (200), (220), and (312) planes, indicating high phase purity and crystallinity. These structural advantages are expected to reduce recombination losses, positioning TF-2 as the most promising candidate for high-performance CZTS solar cells, as discussed in the following section.

Table 2 Elemental composition of the pure CZTS precursor film (PF) for before sulfurization and CZTS thin film (TF) after sulfurization at 650 °C for 20 min examined by EDX analysis

CZTS absorber films	Composition, at%				Ratio	
	Cu	Zn	Sn	S	Cu/(Zn + Sn)	Zn/Sn
PF-1	22.9	13.8	12.7	50.3	0.86	1.08
TF-1	22.0	13.5	9.8	54.6	0.94	1.37
PF-2	20.3	16.5	12.3	50.8	0.70	1.34
TF-2	21.4	14.1	9.9	54.4	0.89	1.42
PF-3	21.8	12.1	10.5	55.4	0.96	1.15
TF-3	26.9	15.1	12.4	45.4	0.97	1.21

3.3. CZTS thin films device performance

The fabricated CZTS thin film solar cells were characterized under standard test conditions to evaluate their photovoltaic performance. The solar cells fabricated from the TF-1, TF-2, and TF-3 absorber layers are referred to as SC-1, SC-2, and SC-3, respectively. Fig. 6 presents the statistical distribution of key photovoltaic parameters for the SC-1, SC-2, and SC-3 devices, derived from the *J–V* measurements. Fig. 6a–d shows the statistical distributions of photovoltaic parameters derived from 20 individual cells for each device, providing a comprehensive assessment of performance variations. Among the tested devices, SC-2-fabricated using CuCl, ZnCl_2, $\text{SnCl}_2\cdot 2\text{H}_2\text{O}$, and Tu, exhibited the highest performance. The average short-circuit current density (J_{SC}) and open-circuit voltage (V_{OC}) were 16 mA cm^{-2} and 600 mV, respectively, highlighting the effectiveness of the optimized precursor composition in improving charge carrier dynamics. These performance results align with SEM, Raman, and XRD analyses, which revealed large, well-defined grains and high structural quality. Notably, the highest performing SC-2 device achieved a PCE of 4.1%, sowed corresponding J_{SC}, V_{OC}, and fill factor (FF) values of 20.3 mA cm^{-2}, 607 mV, and 33.0%, respectively, as shown in Fig. 6e. This result is comparable to previous reports on pure CZTS thin films processed in ambient air using DMSO, where a PCE of 4.7% was achieved.[14] Furthermore, the external quantum efficiency (EQE) measurements and bandgap estimations (Fig. S1, (SI)) were used to determine the optical bandgaps of the SC-1, SC-2, and SC-3 absorber layers. The extracted bandgap values were 1.498 eV for SC-1, 1.526 eV for SC-2, and 1.464 eV for SC-3, indicating slight variations in absorber composition and

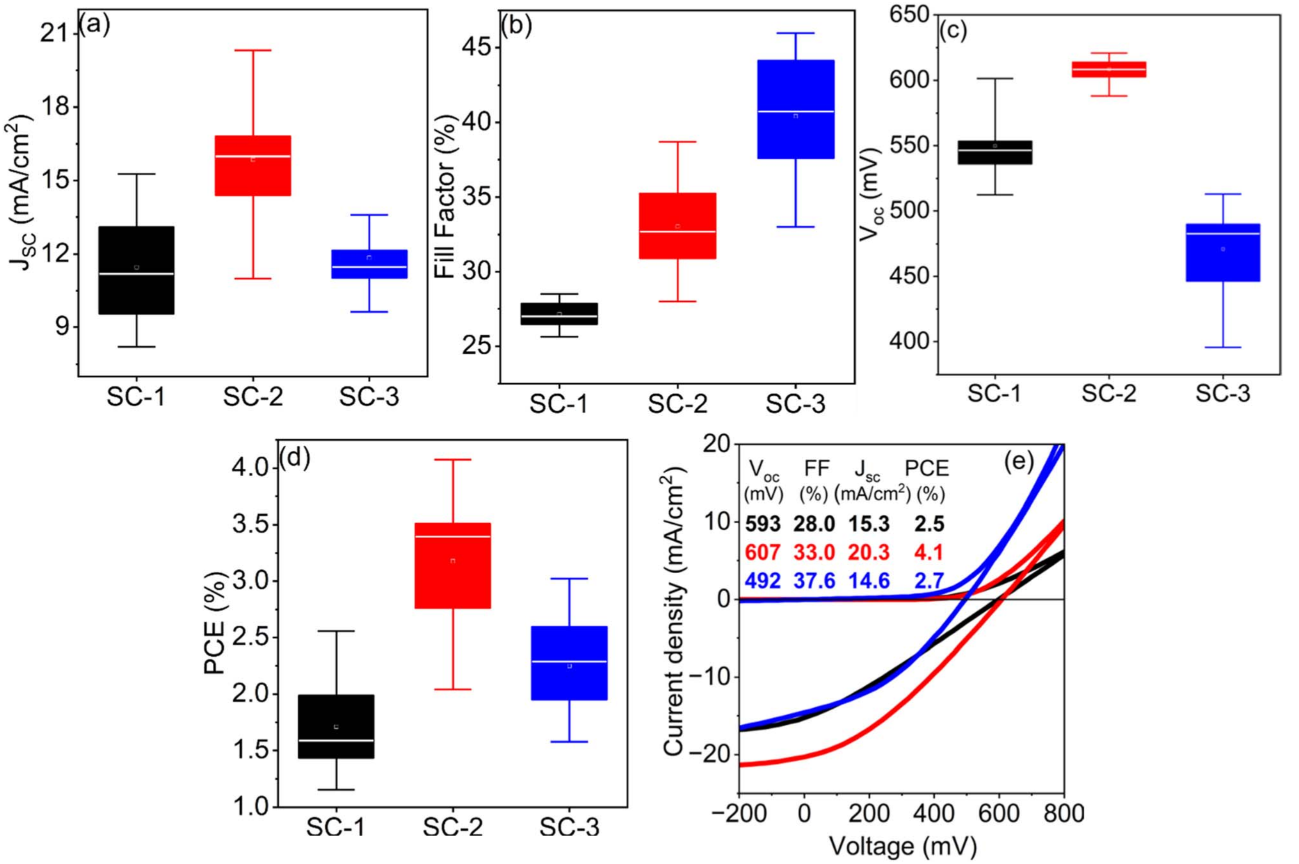

Fig. 6 Box plots of the SC-1, SC-2, and SC-3 devices before post-annealing illustrate the statistical distributions of solar cell parameters: (a) short-circuit current density (J_{SC}), (b) fill factor (FF), (c) open-circuit voltage (V_{OC}), and (d) power conversion efficiency (PCE). (e) Current–voltage (J–V) curves extracted from the highest cell efficiency of SC-1, SC-2, and SC-3 under AM 1.5 illumination (100 mW cm^{-2}), with corresponding V_{OC}, FF, J_{SC}, and PCE values.

crystallinity. It suggests that precursor engineering enables tuning of optoelectronic properties, which is essential for optimizing charge extraction and reducing recombination losses in solution-processed CZTS solar cells.

3.4. Post-annealing of complete devices

Among all investigated devices, SC-2 devices exhibited the highest initial PCE of 4.1%, albeit with a low FF, likely due to resistive losses or non-ideal charge transport mechanisms. A well-established method to enhance FF and overall device performance is post-annealing treatment.[19,20,25] Post-annealing treatment, commonly applied after CBD process for absorber/buffer interfaces, has been reported to improve interfacial quality, mitigate interface defects, and suppress recombination losses in kesterite-based solar cells. Although efficiency improvements are widely observed after post-annealing treatment, the specific effects on V_{OC} and FF vary across different studies.[11,12,19,20,25] Recent work by Wu *et al.*[36] has shown that post-treatment in oxidative environments facilitates elemental interdiffusion and oxygen incorporation, particularly near the heterojunction. This process reduces sulphur vacancy-related defects and improves the p-type nature of the CZTS absorber. These interfacial modifications lead to reduced non-radiative recombination and more favourable band alignment, resulting in improved device performance. In this study, the post-annealing of complete SC-2 device was systematically optimized by varying the annealing duration at 300 °C for 10, 12, and 15 minutes in an ambient air. The devices were labelled SC2-0 min, SC2-10 min, SC2-12 min, and SC2-15 min according to their respective annealing durations. The annealing process was performed on the fully fabricated Mo/CZTS/CdS/i-ZnO/ITO device structure, following a previously reported methodology for CZTS devices.[25] Importantly, annealing was conducted without removing the i-ZnO layer, using a hotplate and graphite box under ambient air.

Fig. 7a–d presents the statistical distribution of key CZTS solar cell parameters as a function of annealing duration, averaged over 20 cells to ensure statistical reliability and reproducibility. A slight increase in J_{SC} was observed across all devices, consistent with previous reports.[11,12,19,20,25] Both FF and PCE also improved significantly (Fig. 7b and d). After 10 minutes annealing at 300 °C (SC2-10 min), PCE and FF improved to 7.0% and 52.2%, with J_{SC} of 21.3 mA cm^{-2} and V_{OC} of 628 mV. Notably, V_{OC} increased linearly with longer annealing durations, reaching a maximum value of 688 mV for SC-15 min device (Fig. 7c). However, extending the annealing time

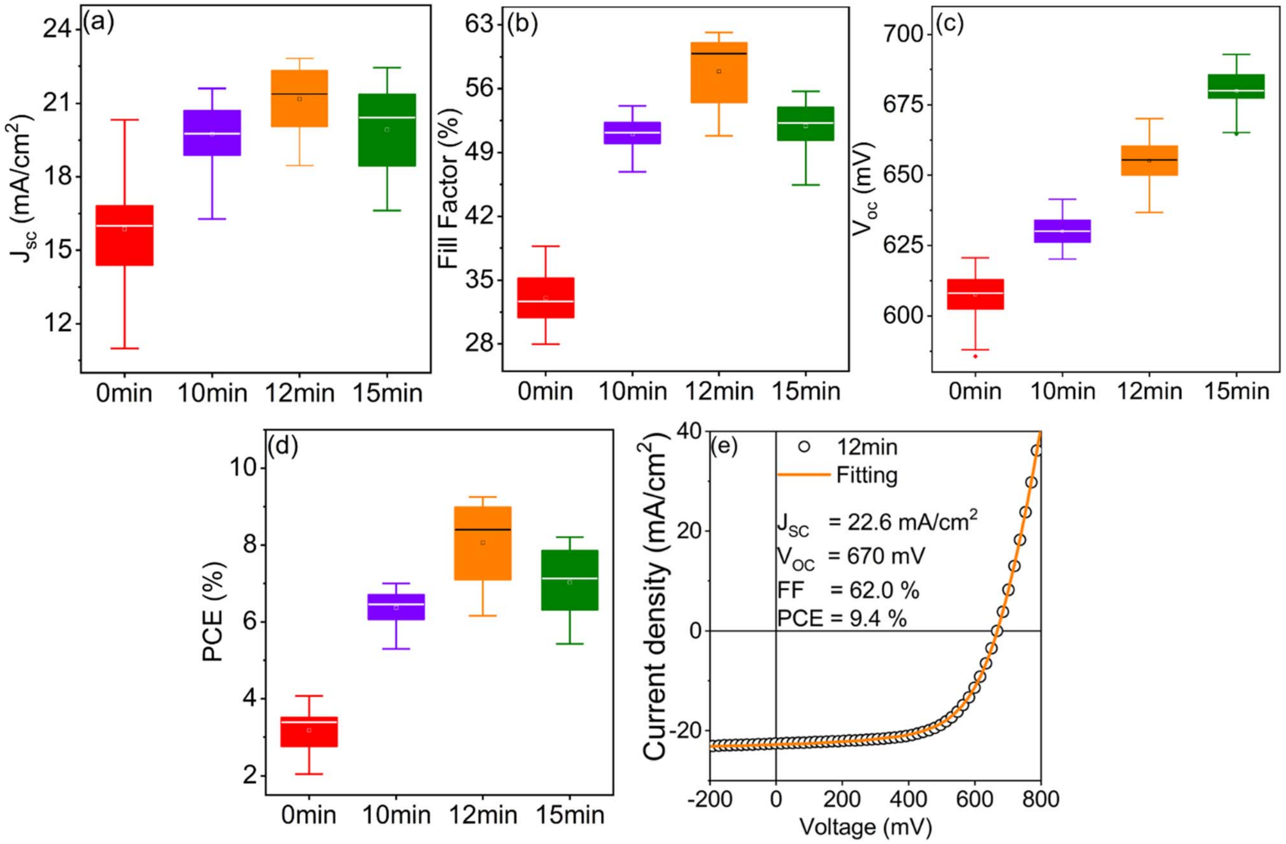

Fig. 7 Plots of solar cell output parameters: (a) J_{SC}, (b) FF, (c) V_{OC}, and (d) PCE for SC2 device subjected to different post-annealing durations of the complete glass/Mo/CZTS/CdS/i-ZnO/ITO structure (SC2-0 min, SC2-10 min, SC2-12 min, and SC2-15 min); (e) J–V curve of the champion device with corresponding fitting result using eqn (9).

to 15 minutes (SC2-15 min) slightly reduced PCE (8.2%) and FF (55.7%), despite higher V_{OC} and slightly lower $J_{SC} = 21.4$ mA cm^{-2}. The optimal annealing condition was determined to be 12 minutes at 300 °C resulting in the highest PCE of 9.4%, with an FF of 62.0%, J_{SC} of 22.6 mA cm^{-2}, and V_{OC} of 670 mV. The champion device's J–V curve and detailed performance metrics are presented in Fig. 7e and Table 3. The champion SC2-12 min device (0.1021 cm^2) achieved the highest reported PCE for pure CZTS solar cells fabricated from DMSO-based solutions under ambient conditions.

For further analysis, the J–V characteristics were fitted using a single-diode model to extract key solar cell parameters as follows:[37]

$$J = J_0\left\{\exp\left[\frac{q(V + JR_s)}{nkT}\right] - 1\right\} + \frac{V + JR_s}{R_{sh}} - J_L \tag{9}$$

where J_0 is the saturation and J_L the photogenerated current densities. The thermal energy is expressed as kT, where T is the absolute temperature and k is the Boltzmann constant. The non-ideal behaviour of the solar cell is explained by the diode ideality factor n, the series resistance R_s, and the parallel resistance R_{sh}.

The R_{sh} and R_s are critical parameters influencing the FF and overall performance of CZTS solar cells. These resistances were extracted from J–V curve fitting to assess the impact of device post-annealing on electrical transport properties, as

Table 3 Comprehensive performance parameters extracted from the highest cell efficiency of SC2-0 min, SC2-10 min, SC2-12 min, and SC2-15 min CZTS solar

SC2	J_{SC} [mA cm^{-2}]	$J_{SC}{}^a$ [mA cm^{-2}]	V_{OC} [mV]	FF [%]	PCE [%]	n	J_0 [A cm^{-2}]	R_{sh} [Ω cm^2]	R_s [Ω cm^2]	E_U [meV]	E_g^* [eV]
0 min	20.3	16.4	607	33.0	4.1	3.0	8.9×10^{-6}	493.8	16.8	42.4	1.526
10 min	21.3	17.8	628	52.2	7.0	2.9	6.9×10^{-6}	339.1	4.4	41.6	1.446
12 min	22.6	19.7	670	62.0	9.4	2.6	1.2×10^{-6}	412.0	4.0	38.4	1.421
15 min	21.4	19.0	688	55.7	8.2	3.0	7.7×10^{-6}	400.2	4.3	39.6	1.455

[a] is the integrated J_{SC} from EQE.

summarized in Table 3. Prior to annealing, the as-fabricated device exhibited a high R_s of 16.8 Ω cm^2, indicating inefficient charge transport. Annealing at 300 °C for 10 minutes substantially reduced R_s to 4.4 Ω cm^2, significantly improving carrier extraction, while R_{sh} slightly decreased from 493.8 Ω cm^2 to 339.1 Ω cm^2. Extending the annealing duration to 12 minutes resulted in the lowest R_s of 4.0 Ω cm^2, along with a moderate increase in R_{sh} to 412.0 Ω cm^2, indicating improved defect passivation and enhanced charge transport. However, extending the annealing to 15 minutes caused a slight increase in R_s to 4.3 Ω cm^2 and a notable decrease in R_{sh} to 400.2 Ω cm^2, suggesting to possible interfacial degradation or enhanced defect-related recombination.

To further investigate charge transport and recombination dynamics in CZTS solar cells, the ideality factor (n) was analysed. The as-fabricated device (SC2-0 min) exhibited an ideality factor of 3.0, indicating dominant Shockley–Read–Hall (SRH) recombination *via* deep defect states within the bulk or at grain boundaries. After 10 minutes of annealing, n slightly decreased to 2.9, suggesting reduced trap-assisted recombination due to improved film crystallinity and defect passivation. The lowest n of 2.6 was observed for the SC2-12 min device, correlating with the optimal R_s (4.0 Ω cm^2) and enhanced R_{sh} (412.0 Ω cm^2). These results indicate that moderate post-annealing of the device effectively passivates defects and enhances charge carrier transport. However, annealing for 15 minutes increased the ideality factor to 3.0, indicating a resurgence of recombination losses, likely due to interfacial degradation or excessive grain growth. This trend is supported by the behaviour of the reverse saturation current density (J_0), a key indicator of recombination losses and junction quality. The as-fabricated device exhibited a J_0 of 8.9×10^{-6} A cm^{-2}, reflecting significant defect-mediated recombination. After 10 minutes of annealing, J_0 decreased to 6.9×10^{-6} A cm^{-2}, due to enhanced crystallinity and heterojunction quality. The lowest J_0 (1.2×10^{-6} A cm^{-2}), along with the highest efficiency (9.4%), was achieved with 12 minutes annealed sample, indicating to reduced non-radiative recombination. Further annealing to 15 min resulted in an increased J_0 to 7.7×10^{-6} A cm^{-2}, likely due to interfacial degradation.

In summary, post-annealing of the complete Mo/CZTS/CdS/i-ZnO/ITO device structure at 300 °C for 12 minutes effectively improved electrical transport properties by reducing R_s, suppressing recombination losses, and enhancing photovoltaic efficiency. These findings provide a straightforward yet effective strategy for improving the performance of solution-processed CZTS solar cells fabricated under ambient air.

To analyse the impact of post-annealing of device on the optical response, external quantum efficiency (EQE) measurements were carried out for SC2-0 min, SC2-10 min, SC2-12 min, and SC2-15 min devices. EQE is a widely used method for evaluate optical and electronic losses in solar cells. Near the absorption edge (*i.e.*, photon energies close to the band gap, $E \approx E_g$), the effective band gap energy (E_g^*) can be determined using the relation:[38]

$$\mathrm{EQE} \approx K\alpha L_{\mathrm{eff}} \approx A\left(E - E_g^*\right)^{1/2} \Big/ E \tag{10}$$

where A is a constant incorporating energy-independent parameters, $L_{\mathrm{eff}} = w + L_d$ represents the effective diffusion length, with L_d as the minority carrier diffusion length and w is the depletion width. α is the absorption coefficient, and constant K is unity in absolute measurements. By plotting $(\mathrm{EQE} \times E)^2$ *vs.* E as presented in Fig. 8b, the linear segment allows extraction of effective band gap energy E_g^*. Bandgap values extracted from EQE fitting were 1.526, 1.446, 1.421, and 1.455 eV for the SC2-0 min, SC2-10 min, SC2-12 min, and SC2-15 min devices, respectively. After 10 minutes of annealing, the bandgap narrowed to 1.446 eV. The SC2-12 min device exhibited the lowest bandgap (1.421 eV), corresponding with its highest PCE (9.4%) and lowest J_0, indicating enhanced junction quality and reduced recombination. The observed decrease in bandgap following post-annealing may be attributed to Cd diffusion into the CZTS absorber, which aligns with previous reports.[12,19,25,36,39–41] In addition, the decreased bandgap is also attributed by Cd-grading CZTS, meaning that post-annealing device may create Cu_2S between CdS and CZTS, Cu_2S and band-gap-graded CZTS together determines the final bandgap.[41]

In Fig. 8a, current collection in the 380–500 nm spectral range improved slightly with increased post-annealing duration, suggesting enhanced carrier extraction and light absorption due to improved crystallinity and interface quality. Notably, the device annealed for 15 minutes showed a significant improvement in current collection between 420–480 nm, which may indicate a reduction in buffer layer thickness with prolonged annealing.[36,41,42] Additionally, several studies have reported that post-annealing of device can also promote the diffusion of indium (In), leading to its incorporation not only within the CdS layer but also, in trace amount, within the absorber layer.[25] This interdiffusion modifies the absorber composition, influences band alignment, and contributes to reduced recombination losses.[19,25] For instance, Xu *et al.*[20] demonstrated that In was intentionally introduced into the CdS buffer layer, it was shown to increase the donor concentration and enhance crystallinity, thus improving electron transport and extraction. When combined with a low-temperature junction heat treatment (JHT), this approach facilitated impurity migration from the buffer to the absorber, improved lattice matching, and significantly reduced interfacial defects. As a result, the CdS:In/CZTSSe-based device achieved a PCE of 14.5%, with a notable reduction in V_{OC} deficit and enhancement of the fill factor. Subsequently, the integrated J_{SC} from the EQE spectra was also presented in Fig. 8a and summarized in Table 3. In all cases, the integrated J_{SC} values were lower than those obtained from the J–V measurements. This discrepancy is primarily attributed to differences in measurement conditions, including lower light intensity during EQE measurements and the absence of bias light, as well as possible spectral mismatch between the actual solar simulator spectrum and the standard AM1.5 G spectrum used in theoretical calculations.

To characterize the band tailing behaviour in post-annealed CZTS solar cells, the Urbach energy (E_U) was calculated to evaluate sub-band gap absorption, using EQE data for each

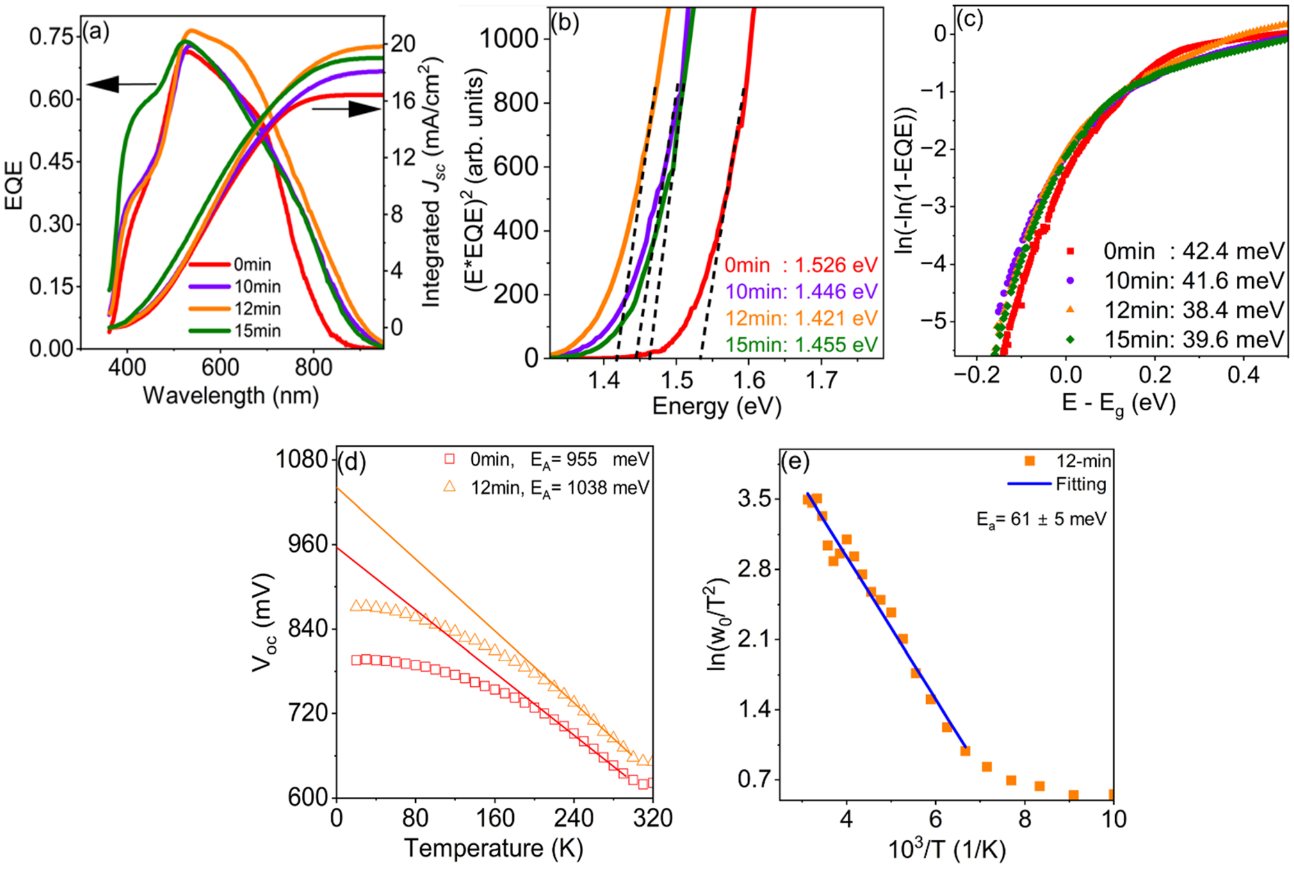

Fig. 8 (a) External quantum efficiency (EQE) spectra and integrated J_{SC} from EQE of CZTS solar cells subjected to post-annealing for various durations (SC2-0 min, SC2-10 min, SC2-12 min, and SC2-15 min) and (b) extracted bandgaps (E_g^*) of the corresponding absorber layers. (c) Urbach energy (E_U) plots derived from EQE data, indicating sub-bandgap tail states. (d) Temperature dependent V_{OC} curves for SC2-0 min and SC2-12 min devices, used to determine activation energy (E_A) from the extrapolated y-axis intercept at $T = 0$ K. (e) Thermal admittance spectroscopy of the SC2-12 min device, revealing defect state energetics.

device. The calculation, developed by Troviano *et al.*,[43] employs the following relation:

$$\ln[-\ln(1-\text{EQE})] = \ln\ a + \frac{h\nu}{E_U} \tag{11}$$

where a is a fitting constant independent of photon energy, $h\nu$ is the photon energy, and E_U-1 corresponds to the slope of the linear region. As presented in Fig. 8c, the E_U values decreased from 42.4 meV (SC2-0 min) and 41.6 meV (SC2-10 min) to 38.4 meV (SC2-12 min), before slightly increasing to 39.6 meV (SC2-15 min). This trend confirms that moderate device annealing particularly at 12 minutes effectively passivates sub-bandgap defects and reduces tail-state density. The higher E_U in the unannealed device indicates higher structural disorder and defect concentration, which are known to promote non-radiative recombination and limit V_{oc} and the performance. Conversely, the lower E_U in SC2-12 min device highlights the optimal annealing condition that minimizes band tailing and enhances charge carrier collection.

To gather more information about the electrical behaviour of the cells, the temperature-dependent J–V measurements were performed under illumination. The behaviour of the V_{OC} of the cells as a function of the temperature V_{OC} (T) is shown in Fig. 8d and can be described by equation:[38]

$$V_{OC} = \frac{E_A}{q} - \frac{nkT}{q}\ln\left(\frac{J_{00}}{J_L}\right) \tag{12}$$

where E_A is the activation energy, q is the elementary charge, n is the ideality factor, k is the Boltzmann constant, T is the temperature, J_{00} is the reverse saturation current prefactor and J_L is the light generated photocurrent density. In the temperature range of 20–300 K, the V_{OC} *versus* T shows linear behaviour. The extrapolation of this linear part to $T = 0$ K indicates the activation energy E_A.

As shown in Fig. 8d, the unannealed SC2-0 min device exhibited E_A of 955 meV, while the SC2-12 min device showed an increased E_A of 1038 meV. This indicates that post-annealing of complete device led to a modest reduction in recombination losses, which remain primarily limited by the absorber/buffer interface as E_A is still lower than E_g, indicating to interface recombination.[12,29,44] The increase in E_A highlights the role of post-annealing in passivating interface traps and enhancing band alignment at the CZTS/CdS interface.[45] To further support the enhanced junction quality, Raman spectroscopy was performed on all devices, as shown in Fig. S3 (SI). A progressive increase in the intensity and sharpness of the characteristic CdS vibrational modes was observed with longer annealing durations, indicating improved crystallinity of the CdS buffer layer. These findings suggest the formation of a higher-quality heterojunction interface between CZTS and CdS, which aligns well with previous reports.[21,23]

To further investigate the defect characteristics of the absorber, temperature-dependent admittance spectroscopy was performed on the SC2-12 min record device. The analysis focused on the inflection frequency (ω_0), which follows the relation:[9,29]

$$\omega_0(T) = 2N_{\text{c,v}}v_{\text{th}}\sigma_{\text{n,p}}\exp\left(\frac{-E_\text{a}}{kT}\right) = 2\xi_0T^2\exp\left(\frac{-E_\text{a}}{kT}\right) \tag{13}$$

where ω_0 is the freeze-out frequency ($2\pi f$), ξ_0 a temperature-independent pre-factor, and E_a is the defect activation energy. By rearranging eqn (13), the activation energy can be extracted from the temperature dependence of the capacitance spectra. Specifically, plotting (ω_0/T^2) *versus* $1000/T$ yields a linear relationship described by:

$$\ln\left(\frac{\omega_0}{T^2}\right) = -\frac{E_\text{a}}{k\times1000}\frac{1000}{T} + \ln(2\xi_0) \tag{14}$$

The slope of the linear fit corresponds to $-E_\text{a}/k \times 1000$, from which the activation energy E_a of a defect level can be calculated using $E_\text{a} = -\text{slope} \times k \times 1000$. More detailed information on the admittance spectroscopy calculations was provided in the SI. As shown in the Arrhenius plot (Fig. 8e), the E_a of the SC2-12 min device is 61 meV, significantly lower than the 155 meV reported for monograin-based CZTS.[29] According to first-principles calculations, the V_{Cu} defect has a shallow energy level of 20–66 meV, whereas the Cu_{Zn} antisite is associated with a deeper level of 110–217 meV.[46–48] In experimental studies by using photoluminescence, on disordered CZTS polycrystals $E_\text{a} = 62 \pm 4$ meV was associated to the formation of defect clusters.[49] A very similar activation energy of 63 ± 8 meV was found in CZTSSe, and associated to defect complexes ($\text{V}_{\text{Cu}} + \text{Zn}_{\text{Cu}}$) or ($\text{Zn}_{\text{Sn}} + 2\text{Zn}_{\text{Cu}}$).[50–52] Impedance spectroscopy was conducted over a temperature range of 20 K to 320 K (Fig. S4 (SI). The SC2-12 min device exhibited a complete semicircular Nyquist plot, indicative of efficient charge transport and reduced interfacial recombination. These features are consistent with the device's low R_s of 4.0 Ω cm^2 and moderate R_{sh} of 412.0 Ω cm^2.

Table S2 (SI) provides an overview of post-annealing strategies applied to kesterite solar cells fabricated *via* various deposition methods and thermal environments. Collectively, these studies confirm the critical role of post-annealing in boosting device performance-primarily through improvements in FF, overall PCE, and suppression of interfacial recombination. In the present work, a complete device post-annealing process under ambient air was developed, using a hotplate combined with a closed graphite box. This setup facilitates efficient post-annealing of Mo/CZTS/CdS/i-ZnO/ITO devices at 300 °C for 12 minutes. The resulting devices exhibited a notable performance improvement, with PCE increasing from 4.1% to 9.4%, and FF from 33.0% to 62.0%. While this manuscript was in preparation, Liang's group[36] reported high-efficiency air-solution-processed pure-CZTS solar cells using MOE, along with varied post-annealing conditions. In comparison, our study demonstrates, for the first time, a comparable achievement using DMSO as the solvent under ambient air. These findings indicate that air-solution-processed pure-CZTS absorber layers are compatible with vacuum-based device fabrication, enabling high-efficiency outcomes. Moreover, our results highlight the potential of optimized post-annealing strategies to overcome the inherent challenges of air processing, paving the way for scalable and eco-friendly fabrication of high-performance kesterite photovoltaics.

4. Conclusion

In summary, we demonstrated high-efficiency, solution-processed CZTS solar cells using DMSO as the solvent under ambient air, achieving a power conversion efficiency of 9.4% through post-annealing of the complete device. From a precursor engineering perspective, we showed that optimizing the precursor composition effectively eliminated worm-like surface patterns and suppressed the formation of Cu_2S secondary phases. The SC-2 device prepared using CuCl, ZnCl_2, $\text{SnCl}_2\cdot2\text{H}_2\text{O}$, and thiourea, initially achieved a modest PCE of 4.1% and a low FF of 33.0%. Post-annealing at 300 °C for 12 minutes on a hotplate within a closed graphite box enhanced device performance, increasing the PCE to 9.4% and FF to 62.0%. These improvements are attributed to enhanced charge transport, reduced series resistance, and suppression of deep-level defects and recombination. Overall, this study demonstrates a simple, scalable, glovebox-free strategy for boosting the FF and efficiency of air-processed CZTS solar cells. To the best of our knowledge, this represents the highest reported efficiency for pure CZTS solar cells with absorbers fabricated using DMSO as solvent under ambient air conditions, offering a promising path toward sustainable, low-cost thin-film photovoltaic technologies.

Author contributions

A. N.: conceptualization, data curation, formal analysis, investigation, methodology, visualization, validation, investigation, writing – original draft, writing – review and editing. M. P. and M. D.: writing – review & editing, formal analysis. J. K.: formal analysis, writing – review & editing, software. A. S., R. K., R. J. and V. M.: methodology. M. G.-K.: writing – review & editing, formal analysis, funding acquisition, project administration. M. K.-K.: writing – original draft, writing – review & editing, formal analysis, methodology, funding acquisition, project administration. Y. G.: writing – review & editing, formal analysis. E. S.: formal analysis, funding acquisition, project administration.

Conflicts of interest

The authors declare no conflict of interest.

Data availability

The data supporting the findings of this study, including raw characterization data, photovoltaic performance parameters, and associated analysis scripts, are available at Zenodo data repository: **https://doi.org/10.5281/zenodo.15599572**.

Supplementary information is available. See DOI: **https://doi.org/10.1039/d5ta04554a**.

Acknowledgements

This work was supported by the European Union through the European Regional Development Fund (Project TK210) and the Estonian Research Council (Grants PRG1023, PRG1815). The research was carried out using the NAMUR+ core facility, funded by the Estonian Research Council (Projects TT13, TTK26). This project also received funding from the European Union's Horizon research and innovation programme under grant agreement number 101151487 (LEKPV); and by the Spanish Ministry of Science and Innovation project PID2023-148976OB-C41 (CURIO-CITY); and by the Cost Association project number CA-706 21148 (Renew-PV). This work is also part of Maria de Maeztu Units of Excellence 707 Programme CEX2023-001300 M/ funded by MICIU/AEI/10.13039/501100011033. The authors from UPC belong to the Micro and Nanotechnologies for Solar Energy 709 Group (MNTSolar) Consolidated Research Group of the "Generalitat de Catalunya" 710 (2021 SGR 01286). E. S. acknowledges the ICREA Academia program.

References

1 D. B. Mitzi, O. Gunawan, T. K. Todorov, K. Wang and S. Guha, *Sol. Energy Mater. Sol. Cells*, 2011, **95**, 1421–1436.

2 Y. E. Romanyuk, S. G. Haass, S. Giraldo, M. Placidi, D. Tiwari, D. J. Fermin, X. Hao, H. Xin, T. Schnabel, M. Kauk-Kuusik, P. Pistor, S. Lie and L. H. Wong, *J. Phys.: Energy*, 2019, **1**, 044004.

3 Y. Li, C. Cui, H. Wei, Z. Shao, Z. Wu, S. Zhang, X. Wang, S. Pang and G. Cui, *Adv. Mater.*, 2024, **36**, 1–8.

4 K. Yin, J. Wang, L. Lou, F. Meng, X. Xu, B. Zhang, M. Jiao, J. Shi, D. Li, H. Wu, Y. Luo and Q. Meng, *Nat. Energy*, 2025, **10**, 205–214.

5 J. Fu, J. Yang, W. Dong, S. Ren, H. Zhu, Y. Wang, J. Hao, J. Wu, R. Wang, D. Zhao, Y. Zhang and Z. Zheng, *J. Mater. Chem. A*, 2023, **12**, 545–566.

6 W. Wang, M. T. Winkler, O. Gunawan, T. Gokmen, T. K. Todorov, Y. Zhu and D. B. Mitzi, *Adv. Energy Mater.*, 2014, **4**, 1–5.

7 W. Ki and H. W. Hillhouse, *Adv. Energy Mater.*, 2011, **1**, 732–735.

8 H. Xin, J. K. Katahara, I. L. Braly and H. W. Hillhouse, *Adv. Energy Mater.*, 2014, **4**, 1–5.

9 S. G. Haass, M. Diethelm, M. Werner, B. Bissig, Y. E. Romanyuk and A. N. Tiwari, *Adv. Energy Mater.*, 2015, **5**, 1–7.

10 Y. Gong, Y. Zhang, E. Jedlicka, R. Giridharagopal, J. A. Clark, W. Yan, C. Niu, R. Qiu, J. Jiang, S. Yu, S. Wu, H. W. Hillhouse, D. S. Ginger, W. Huang and H. Xin, *Sci. China Mater.*, 2021, **64**, 52–60.

11 Y. Gong, Y. Zhang, Q. Zhu, Y. Zhou, R. Qiu, C. Niu, W. Yan, W. Huang and H. Xin, *Energy Environ. Sci.*, 2021, **14**, 2369–2380.

12 Y. Gong, Q. Zhu, B. Li, S. Wang, B. Duan, L. Lou, C. Xiang, E. Jedlicka, R. Giridharagopal, Y. Zhou, Q. Dai, W. Yan, S. Chen, Q. Meng and H. Xin, *Nat. Energy*, 2022, **7**, 966–977.

13 Y. Gong, A. Jimenez-Arguijo, A. G. Medaille, S. Moser, A. Basak, R. Scaffidi, R. Carron, D. Flandre, B. Vermang, S. Giraldo, H. Xin, A. Perez-Rodriguez and E. Saucedo, *Adv. Funct. Mater.*, 2024, **2404669**, 1–11.

14 S. Engberg, F. Martinho, M. Gansukh, A. Protti, R. Küngas, E. Stamate, O. Hansen, S. Canulescu and J. Schou, *Sci. Rep.*, 2020, **10**, 1–14.

15 Y. Bai, Y. Wang, R. Liu, Y. He, Y. Zhang, C. Liu, H. Luan, Y. Yang and C. Zhu, *Sol. Energy Mater. Sol. Cells*, 2024, **274**, 16–18.

16 Y. Sun, S. Qin, D. Ding, H. Gao, Q. Zhou and X. Guo, *Chem. Eng. J.*, 2023, **455**, 140596.

17 Y. Zhao, C. Xu, N. Yu, Z. Zhou, Y. Chen, X. Hu, Y. Zhang and S. Wang, *Sol. Energy*, 2023, **258**, 294–303.

18 Y. Zhao, X. Han, L. Chang, J. Li, C. Dong, Y. Fang and J. Li, *Sol. Energy Mater. Sol. Cells*, 2018, **179**, 427–434.

19 C. Yan, J. Huang, K. Sun, S. Johnston, Y. Zhang, H. Sun, A. Pu, M. He, F. Liu, K. Eder, L. Yang, J. M. Cairney, N. J. Ekins-Daukes, Z. Hameiri, J. A. Stride, S. Chen, M. A. Green and X. Hao, *Nat. Energy*, 2018, **3**, 764–772.

20 J. Xu, C. Cui, D. Kou, Z. Wu, W. Zhou, Z. Zhou, S. Yuan, Y. Qi, Y. Meng, L. Han and S. Wu, *ACS Energy Lett.*, 2024, **9**, 4939–4946.

21 M. G. Sousa, A. F. da Cunha, J. P. Teixeira, J. P. Leitão, G. Otero-Irurueta and M. K. Singh, *Sol. Energy Mater. Sol. Cells*, 2017, **170**, 287–294.

22 M. Neuschitzer, Y. Sanchez, T. Olar, T. Thersleff, S. Lopez-Marino, F. Oliva, M. Espindola-Rodriguez, H. Xie, M. Placidi, V. Izquierdo-Roca, I. Lauermann, K. Leifer, A. Pérez-Rodriguez and E. Saucedo, *Chem. Mater.*, 2015, **27**, 5279–5287.

23 M. Gansukh, F. Martinho, M. Espindola, S. Engberg, J. Schou and S. Canulescu, *Sci. Rep.*, 2024, **14**, 1–7.

24 Y. Liu, S. Wang and Y. Zhang, *JPhys Energy*, 2024, **6**, 1–23.

25 Z. Su, G. Liang, P. Fan, J. Luo, Z. Zheng, Z. Xie, W. Wang, S. Chen, J. Hu, Y. Wei, C. Yan, J. Huang, X. Hao and F. Liu, *Adv. Mater.*, 2020, **32**, 1–12.

26 S. Gao, Y. Zhang, J. Ao, X. Li, S. Qiao, Y. Wang, S. Lin, Z. Zhang, D. Wang, Z. Zhou, G. Sun, S. Wang and Y. Sun, *Sol. Energy Mater. Sol. Cells*, 2018, **182**, 228–236.

27 C. Malerba, M. Valentini and A. Mittiga, *Sol. RRL*, 2017, **1**, 1–11.

28 B. Duan, L. Guo, Q. Yu, J. Shi, H. Wu, Y. Luo, D. Li, S. Wu, Z. Zheng and Q. Meng, *J. Energy Chem.*, 2020, **40**, 196–203.

29 M. Kauk-Kuusik, K. Timmo, K. Muska, M. Pilvet, J. Krustok, R. Josepson, G. Brammertz, B. Vermang, M. Danilson and M. Grossberg, *ACS Appl. Energy Mater.*, 2021, **4**, 12374–12382.

30 M. Kauk-Kuusik, K. Timmo, M. Pilvet, K. Muska, M. Danilson, J. Krustok, R. Josepson, V. Mikli and

M. Grossberg-Kuusk, *J. Mater. Chem. A*, 2023, **11**, 23640–23652.

31 I. D. Olekseyuk, I. V. Dudchak and L. V. Piskach, *J. Alloys Compd.*, 2004, **368**, 135–143.

32 S. Temgoua, R. Bodeux and N. Naghavi, *Sol. Energy Mater. Sol. Cells*, 2017, **172**, 160–167.

33 E. Indubala, S. Sarveshvaran, V. Sudha, A. Y. Mamajiwala and S. Harinipriya, *Sol. Energy*, 2018, **173**, 215–224.

34 A. Xu, X. Li, H. Liu, C. Xiang, C. Ma, Y. Li, X. Pan, W. Yan, S. Wang, W. Huang and H. Xin, *Small*, 2025, **21**, 1–9.

35 M. Kauk, K. Muska, M. Altosaar, J. Raudoja, M. Pilvet, T. Varema, K. Timmo and O. Volobujeva, *Energy Procedia*, 2011, **10**, 197–202.

36 T. Wu, S. Chen, Z. Su, Z. Wang, P. Luo, Z. Zheng, J. Luo, H. Ma, X. Zhang and G. Liang, *Nat. Energy*, 2025, **10**, 630–640.

37 S. Suckow, T. M. Pletzer and H. Kurz, *Prog. Photovolt: Res. Appl.*, 2014, **22**, 494–501.

38 E. Kask, J. Krustok, S. Giraldo, M. Neuschitzer, S. López-Marino and E. Saucedo, *J. Phys. D Appl. Phys.*, 2016, **49**, 085101.

39 Z. Su, J. M. R. Tan, X. Li, X. Zeng, S. K. Batabyal and L. H. Wong, *Adv. Energy Mater.*, 2015, **5**, 2–8.

40 M. Pilvet, M. Kauk-Kuusik, M. Altosaar, M. Grossberg, M. Danilson, K. Timmo, A. Mere and V. Mikli, *Thin Solid Films*, 2015, **582**, 180–183.

41 H. Guo, R. Meng, G. Wang, S. Wang, L. Wu, J. Li, Z. Wang, J. Dong, X. Hao and Y. Zhang, *Energy Environ. Sci.*, 2022, **15**, 693–704.

42 G. Kartopu, B. L. Williams, V. Zardetto, A. K. Gürlek, A. J. Clayton, S. Jones, W. M. M. Kessels, M. Creatore and S. J. C. Irvine, *Sol. Energy Mater. Sol. Cells*, 2019, **191**, 78–82.

43 M. Troviano and K. Taretto, *Sol. Energy Mater. Sol. Cells*, 2011, **95**, 821–828.

44 J. Krustok, K. Timmo, M. Kauk-Kuusik and M. Grossberg-Kuusk, *Appl. Phys. Lett.*, 2023, **123**, 1–5.

45 S. Deng, S. Wang, Y. Wang, Q. Xiao, Y. Meng, D. Kou, W. Zhou, Z. Zhou, Z. Zheng and S. Wu, *J. Energy Chem.*, 2024, **95**, 77–85.

46 S. Chen, X. G. Gong, A. Walsh and S. H. Wei, *Appl. Phys. Lett.*, 2010, **96**, 4–7.

47 P. A. Fernandes, A. F. Sartori, P. M. P. Salomé, J. Malaquias, A. F. da Cunha, M. P. F. Graça and J. C. González, *Appl. Phys. Lett.*, 2012, **100**, 233504.

48 S. Chen, A. Walsh, X. G. Gong and S. H. Wei, *Adv. Mater.*, 2013, **25**, 1522–1539.

49 M. Grossberg, J. Krustok, T. Raadik, M. Kauk-Kuusik and J. Raudoja, *Curr. Appl. Phys.*, 2014, **14**, 1424–1427.

50 S. Campbell, Y. Qu, L. Bowen, P. Chapon, V. Barrioz, N. S. Beattie and G. Zoppi, *Sol. Energy*, 2018, **175**, 101–109.

51 M. Grossberg, J. Krustok, C. J. Hages, D. M. Bishop, O. Gunawan, R. Scheer, S. M. Lyam, H. Hempel, S. Levcenco and T. Unold, *J. Phys.: Energy*, 2019, **1**, 044002.

52 C. Cui, D. Kou, W. Zhou, Z. Zhou, S. Yuan, Y. Qi, Z. Zheng and S. Wu, *J. Energy Chem.*, 2022, **67**, 555–562.